nature materials

SUPPLEMENTARY INFORMATION

DOI: 10.1038/NMAT4091

Vertical and In-Plane Heterostructures from WS_2/MoS_2 Monolayers

Yongji Gong[1, 2 †], Junhao Lin[3, 4 †], Xingli Wang[5 †] Gang Shi[2], Sidong Lei[2], Zhong Lin[6], Xiaolong Zou[2], Gonglan Ye[2], Robert Vajtai[2], Boris I. Yakobson[2], Humberto Terrones[7], Mauricio Terrones[6, 8], Beng Kang Tay[5], Jun Lou[2], Sokrates T. Pantelides[3, 4], Zheng Liu[5], Wu Zhou[3 *], Pulickel M. Ajayan[1,2 *]

1. Methods

Synthesis of WS_2/MoS_2 vertical heterostructure

In order to synthesize WS_2/MoS_2 vertical stacked bilayer, chemical vapor deposition method (CVD) has been developed. Sulfur (99%, Sigma Aldrich), tungsten (99.99%, Sigma Aldrich) and molybdenum oxide (MoO_3) (99%, Sigma Aldrich) powders were used as S, W and Mo precursors, respectively. The addition of tellurium (99.99%, Sigma Aldrich) was used to accelerate the melting of tungsten powder during the growth. The mass of W, Te, MoO_3 and S was 10 mg, 100 mg, 25 mg and 500 mg, respectively. The ratio of W:Te was about 1:10. Mixed power of tungsten and tellurium was scattered on the SiO_2/Si wafer (285 nm thick SiO_2, Addison Engineering), while MoO_3 powder was put in front of the wafer. The SiO_2/Si wafer with W and Te powders also served as the growth substrate of the heterostructures. 100 sccm (cubic centimeters per minute) argon is used to protect the system from oxygen and carry sulfur vapor from the upstream of the tube during the reaction. The furnace is heated to 850°C in 15 min and cooled down naturally after staying at 850°C (this is the temperature of the reaction area, where the MoO_3, W, Te and substrate are located. The temperature of the sulfur source is at about 200°C.) for another 15 min. The growth is performed under atmospheric pressure. The heating gradient of the furnace is about 40°C/cm from the flat temperature zone to the room temperature zone.

Synthesis of WS_2/MoS_2 in-plane heterostructure

The synthesis of WS_2/MoS_2 in-plane heterostructure is the same as the vertical heterostructure except that the growth temperature is 650°C.

Synthesis of WS_2 and MoS_2

DOI: 10.1038/NMAT4091

Monolayer and bilayer WS_2 were synthesized using the same method as for growing WS_2/MoS_2 vertical bilayer, except that MoO_3 powder was removed. Bilayer MoS_2 was synthesized by CVD method as reported in literature.[1,2]

Sample transfer

All the transfer processes, including TEM sample and WS_2/MoS_2 bilayers made by mechanical transfer in our study, were performed following a poly (methyl methacrylate) (PMMA) (950 PMMA A4, Micro Chem) assisted method. SiO_2 layer was etched by 2M KOH solution after a PMMA thin film was spin-coated on the top of the sample/SiO_2/Si substrate. The lifted off PMMA/sample layer was then transferred onto other substrate and air-dried. PMMA was washed off with acetone and isopropanol.

STEM Z-contrast imaging and chemical analysis

In order to avoid hydrocarbon contamination, the TEM sample of the vertical stacked heterostructure was annealed at 700°C for 2 hours under 10^{-7} torr vacuum, which generated some triangular pits in the film.[3] All TEM samples were baked at 160°C for 8 hours under vacuum before the microscopy experiment. Scanning transmission electron microscopy (STEM) imaging and electron energy-loss spectroscopy (EELS) analysis were performed on an aberration-corrected Nion UltraSTEM-100 operating at 60 kV. The convergence semi-angle for the incident probe was 31 mrad. Z-contrast images were gathered for a half-angle range of ~86-200 mrad. EELS spectra were collected with a collection semi-angle of 48 mrad. The W and Mo chemical maps were obtained by multiple linear least squares (MLLS) fitting of the experimental EELS spectrum image with the reference spectra of W O-edge and Mo N-edge shown in Fig. S8, acquired under the same experimental conditions.

Raman and PL characterization

Raman and PL spectra and the corresponding mappings are performed under 514.5 nm laser excitation (Renishaw inVia) with a power of 20 mW at room temperature. The spot size of the laser is about 1 μm^2. The step size for Raman and PL map is about 0.5 μm.

FET device fabrication and test on vertical stacked WS_2/MoS_2 heterostructures

The geometry of the transportation channel is fabricated by two lithography-etching processes. First, we deliberately patterned and etched out the MoS_2 areas which are not covered by WS_2 or directly used totally covered WS_2/MoS_2 bilayers. After making contacts to the bilayer films, we further patterned the film into a square bar as the red lines indicates (Fig. S14A). The width and length is measured by SEM images.

Metal electrodes (1.5 nm Ti / 30 nm Au) were deposited on both top and side of the bilayer structure to connect with both layers. All electrical measurements are carried out in the probe-station along with an Agilent B1500A Semiconductor Device Analyzer under high vacuum (10^{-5} torr). The mobility is estimated by calculating the linear regime of the transfer characteristics using the equation $\mu_{FE} = \frac{Lg_m}{C_g W V_d}$, **where** $g_m = \frac{\mathrm{d}I_{sd}}{\mathrm{d}V_g}\Big|_{V_{sd}=const}$.[1,2]

Details in the DFT calculations

Density functional theory (DFT) calculations on the band structure of the zigzag and armchair WS_2/MoS_2 interfaces, as shown in Figs. S23 and S24, were carried out under the plane wave code CASTEP[4] with the local density approximation (LDA) considering the Ceperly-Alder-Perdew and Zunger (CA-PZ) functional[5,6]. The Monkhorst-Pack K-point sampling was set to be 8×3×1 and cut off energy of the plane waves was 650 eV. All the structures were relaxed, including the unit cells, until the forces became smaller than 0.03 eV/Å and the energy tolerances were less than 5×10^{-6} eV/atom. A vacuum of 20 Å between the layers was considered to avoid layer interactions. It is important to mention that although DFT underestimates the electronic band gap, it provides good agreement with the optical band gap in semiconducting transition metal dichalcogenides (TMDs). This coincidence allows us to shed light on the general features appearing in the band structure. In addition, in both interfaces (zigzag and armchair), the projected density of states (PDOS) reveals that tungsten d-electrons play a major role close to the valence band maximum, while molybdenum d-electrons exhibit greater presence at the bottom of the conduction band, and in agreement with previous calculations[7].

DOI: 10.1038/NMAT4091

DFT calculations on the band alignment of the WS_2/MoS_2 heterojunction shown in Fig. S25 were performed under the Vienna ab initio simulation package (vasp) with the core-valence interaction described by frozen-core projector augmented wave (PAW) method. The exchange-correlation functional was described by the generalized gradient approximation of Perdew-Burke-Ernzerhof (GGA-PBE). All atoms are allowed to relax until the calculated Hellmann-Feynman force for all atoms is less than 0.01 eV/Å.

For calculations on the energy gain per unit length (α) due to the chemical bonding and energy gain per unit area (β) due to the van der Waal stacking in the discussion of growth mechanism, we choose local density approximation (LDA) to the exchange-correlation functional. We consider the most stable 2H (or AA') stacking as shown in Figure 2G in the main text for the van der Waals energy calculation. The α (β) is calculated by DFT using the routine method on binding energies of two materials divided by the length (area) of the binding region[8-10].

2. Discussion of possible growth mechanism

We proposed the growth of the WS_2/Mos_2 heterostructures follows the chemical reaction equations below:

$$2MoO_3+7S \xrightarrow{650°C} 2MoS_2+3SO_2 \quad (1)$$

$$MoS_2(edge)+W(Te)+2S \xrightarrow{650°C} WS_2/MoS_2(lateral)+Te \quad (2)$$

$$2MoO_3+7S \xrightarrow{850°C} 2MoS_2+3SO_2 \quad (3)$$

$$MoS_2(Surface)+W(Te)+2S \xrightarrow{850°C} WS_2/MoS_2(vertical)+Te \quad (4)$$

Under our growth conditions, MoS_2 always grows first as the bottom layers or at the center (chemical reaction equation (1) or (3)) because of its high nucleation and growth rate during vapor phase reaction. On the other hand, WS_2 nucleation and growth is much slower, due to the low vapor pressure of W and low solubility of W in liquid Te under the 650 - 850°C reaction temperature. Phase diagram (Fig. S4) shows that Te accelerates the melting of tungsten, which then reacts with S to form WS_2 atomic layers. Because of the ultrahigh melting temperature of W on its own, we propose that the growth of WS_2 with W-Te mixed

powder as precursor is a liquid reaction rather than a vapor reaction. This is the reason why we need to place the W-Te mixed powder on the growth substrate directly. The growth under similar synthesis conditions without using Te results in only MoS_2 atomic layers and bulk WS_2 particles (Fig. S1). The large difference in reaction rate gives rise to the vertical stacked or in-plane WS_2/MoS_2 heterostructure rather than the random $Mo_xW_{1-x}S_2$ alloy. For comparison, if WO_3, instead of W-Te, is used as precursor for the growth, we obtain random $Mo_xW_{1-x}S_2$ alloy (Fig. S2), presumably due to the similar sublimation rate of WO_3 and MoO_3.

No Te was detected in the final products. This could be due to the instability of $MoTe_2$ and WTe_2 under sulfur vapor at high temperature. For instance, MoS_2 particles are obtained when annealing $MoTe_2$ monolayer with sulfur at high temperature (600-700˚C). Moreover, when we used MoO_3, S and Te for the growth, we only obtained MoS_2 instead of $MoS_{2-x}Te_x$ alloy, which is consistent with previous theoretical study that $MoS_{2-x}Te_x$ alloy is not stable[11].

Occasionally, we find a very small amount of heterostacks at 650˚C. However, we never find in-plane heterojunctions at 850˚C. At 750 ˚C, we obtain a mixture of both types of heterostructures.

The observed temperature-selective growth can be explained as follows. We propose that the lateral heterostructure grown at low temperature is a kinetic product, while the vertical stacked bilayer at high temperature is a thermodynamic product, which is a general case for temperature selective growth in chemistry[12].

To perform the thermodynamic stability analysis, we adopt the models schematically shown in Fig. S3, with the characteristic length of L for WS_2 flake. Since the edge energies are comparable in these two cases, the energy gain during the growth for in-plane and stacking heterostructures are mainly from edge binding (for in-plane heterostructure) and van der Waals interaction (for vertical stacking heterostructure) between MoS_2 and WS_2 flakes, respectively. The binding energy is linear to the contact length, denoted as αL, where α is the energy gain per unit length due to the chemical bonding and calculated to be 1.62 eV/Å (see

DOI: 10.1038/NMAT4091

Methods). The van der Waals energy is proportional to the contact area between WS_2 and MoS_2 flakes, defined as $\frac{\sqrt{3}}{4}\beta L^2$, where β is the energy gain per unit area due to Van der Waal stacking and $\beta = 0.026$ eV/Å^2 (see Methods), and the factor $\frac{\sqrt{3}}{4}$comes from the triangular shape of the WS_2 flake. For WS_2 flake with L = 1 μm, the energy gain for in-plane and stacking heterostructures are 1.62×10^6 eV and 1.1×10^{10} eV, respectively. As L goes larger, the difference in energy gain becomes larger. Therefore, the stacking heterostructure is thermodynamically favored.

At low temperature (650 ˚C), nucleation and growth of WS_2 is extremely difficult and slow[13]. Attaching WS_2 to the MoS_2 edge with strong chemical bonding, however, results in much smaller nucleation energy than on the surface of MoS_2, which leads to in-plane heterostructure, a kinetic product preferred at low temperature. At high temperature (850 ˚C), the environment would provide enough energy to overcome the nucleation barrier. In this case, the kinetic effect would not be critical and the thermodynamically more stable product becomes preferable. Thus, WS_2/MoS_2 bilayer heterostructure is preferred at this higher temperature. A more detailed exploration of the growth mechanism would require further experimental and theoretical effort.

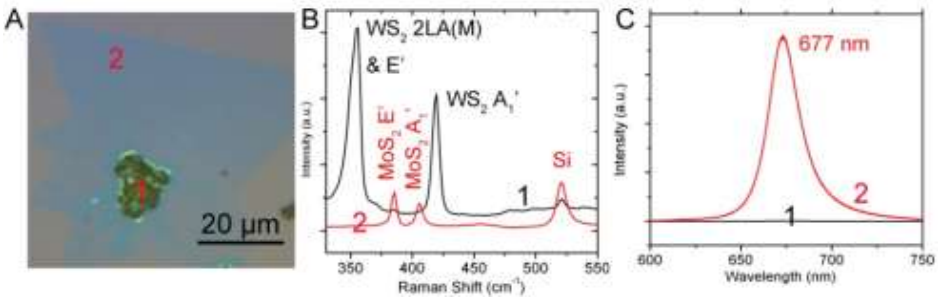

Figure S1. Growth results without using Te. (A) Optical image showing MoS_2 atomic layers (2) and WS_2 bulk particles (1), which is confirmed by the Raman (B) and PL (C) spectra.

DOI: 10.1038/NMAT4091

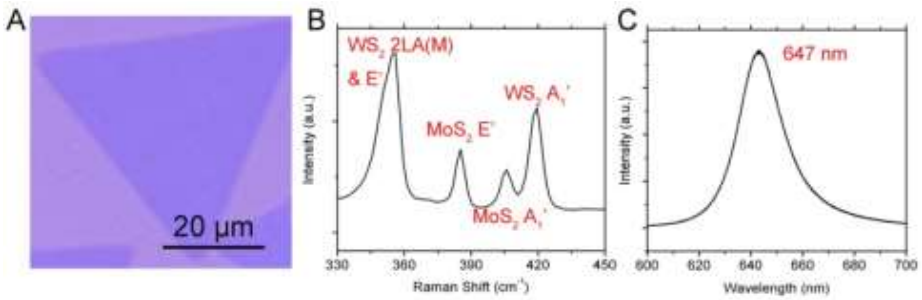

Figure S2. Growth results using WO_3 instead of W/Te as precursor. (A) Optical image showing the formation of uniform monolayer without any interface. (B) Raman spectrum of the as-synthesized monolayer. Both characteristic peaks of MoS_2 and WS_2 are found. (C) PL spectrum of the as-synthesized monolayer. Only one strong peak at 647 nm is observed, which is the feature of a $Mo_xW_{1-x}S_2$ alloy monolayer with $x \sim 0.4$[14].

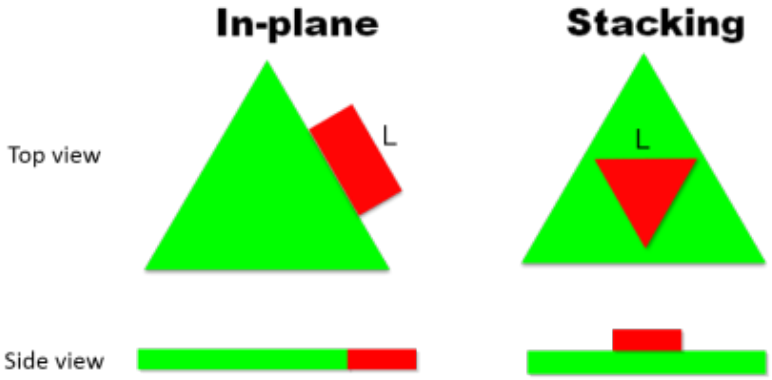

Figure S3. Schematic models for growth mechanisms. The green and red colors represent MoS_2 and WS_2 monolayers, respectively.

DOI: 10.1038/NMAT4091

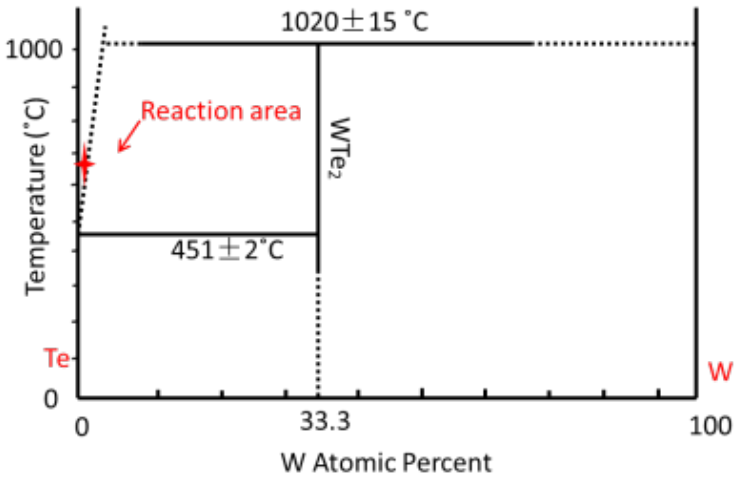

Figure S4. Binary phase diagram of W-Te.[15] The area marked by red arrow shows that W is a little soluble in liquid Te above 450°C. The diagram is adapted from Ref. #11.

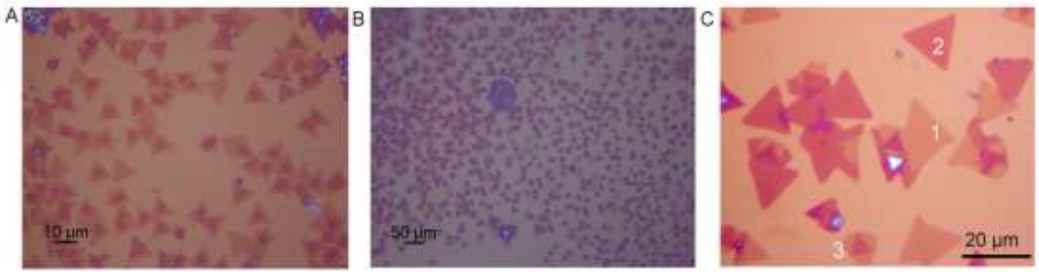

Figure S5. Optical images of WS_2/MoS_2 vertical heterostructures at different magnifications, showing the high yield of this direct-growth method. The regions labeled with "1", "2", and "3" in (C) represent monolayer MoS_2, totally covered WS_2/MoS_2 bilayer, and partially covered WS_2/MoS_2 bilayer with steps, respectively.

DOI: 10.1038/NMAT4091

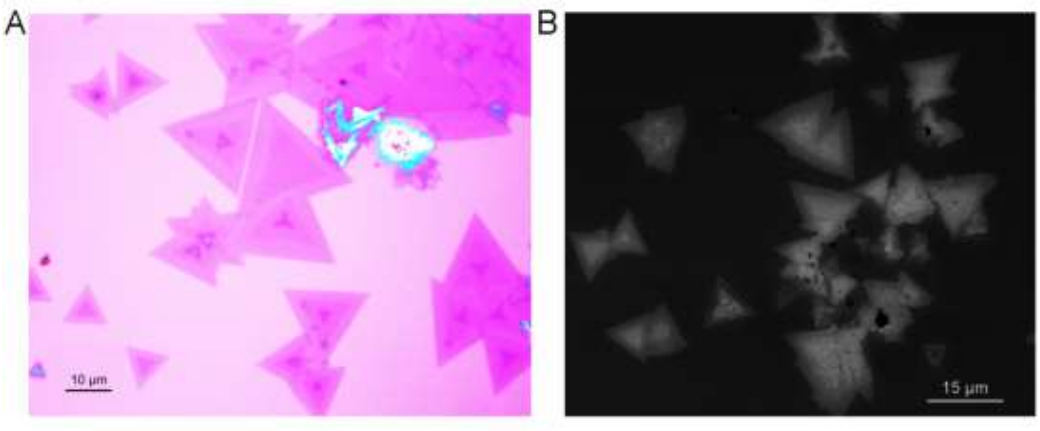

Figure S6. Optical and SEM images at larger-scale showing the high-yield of the WS_2-MoS_2 in-plane heterojunction. The SEM image is shown in reverse contrast.

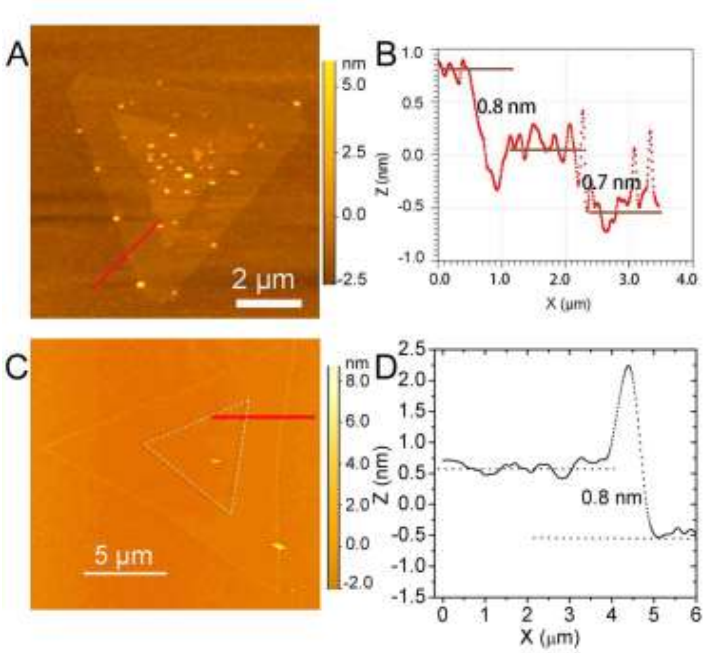

Figure S7. AFM images of the vertical stacked and in-plane heterostructure of WS_2/MoS_2. (A) Typical AFM height topographies of a WS_2/MoS_2 bilayer heterostructure. (B) Height profile along the red line in (A), showing the height difference is around 0.7 nm as approaching from substrate to the monolayer, and from monolayer to bilayer. (C) Typical AFM height topographies of WS_2-MoS_2 in-plane heterojunction. The interface is highlighted by the dashed lines. (D) Height profile along the red line in (C), showing the uniform thickness.

DOI: 10.1038/NMAT4091

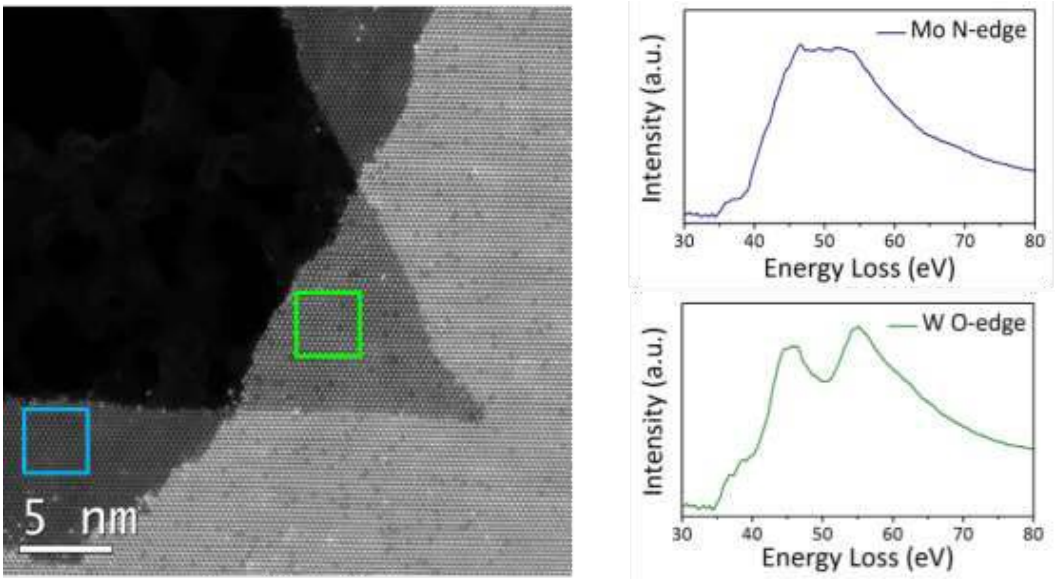

Figure S8. Chemical identity of the two monolayers in the WS_2/MoS_2 vertical stacked bilayer. The chemical identity of each individual layer is confirmed by EELS. EELS spectra (right) collected from the individual MoS_2 and WS_2 monolayers (green and blue squares in the Z-contrast image shown in the left, respectively) show distinct fine structures for Mo N-edge in MoS_2 and W O-edge in WS_2, confirming the presence of the well-separated MoS_2 and WS_2 monolayer.

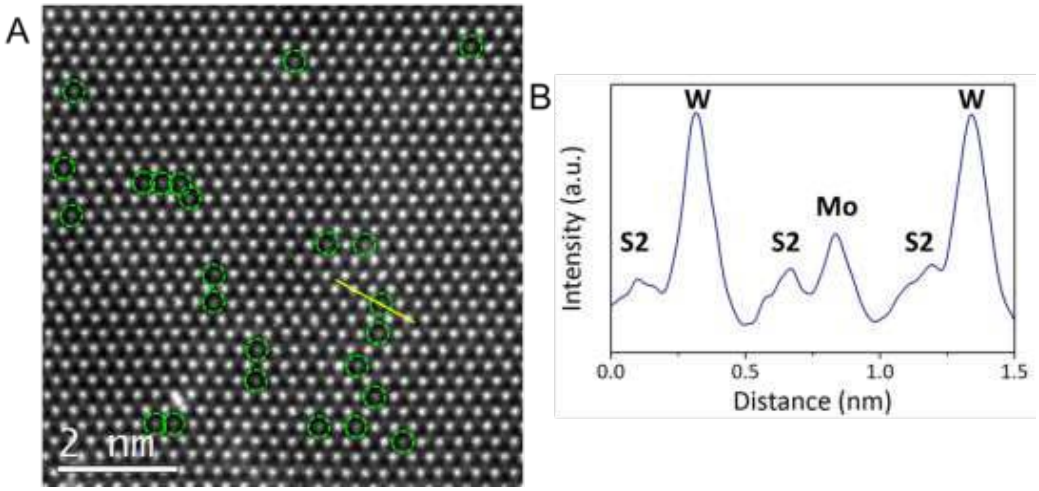

Figure S9. STEM-Z-contrast image analysis of WS_2 monolayer with Mo substitution. (A) Z-contrast image showing some of the metal sites in the monolayer WS_2 having weaker image intensity. (B) Image intensity profile acquired along the yellow line in A, showing the change in image contrast due to substitution of Mo at W site. Using the site-separated histogram analysis method discussed in literature[16], the location of the substituted Mo atoms can be mapped out, as highlighted by the dash green circles, and the local Mo concentration is about 3%.

DOI: 10.1038/NMAT4091

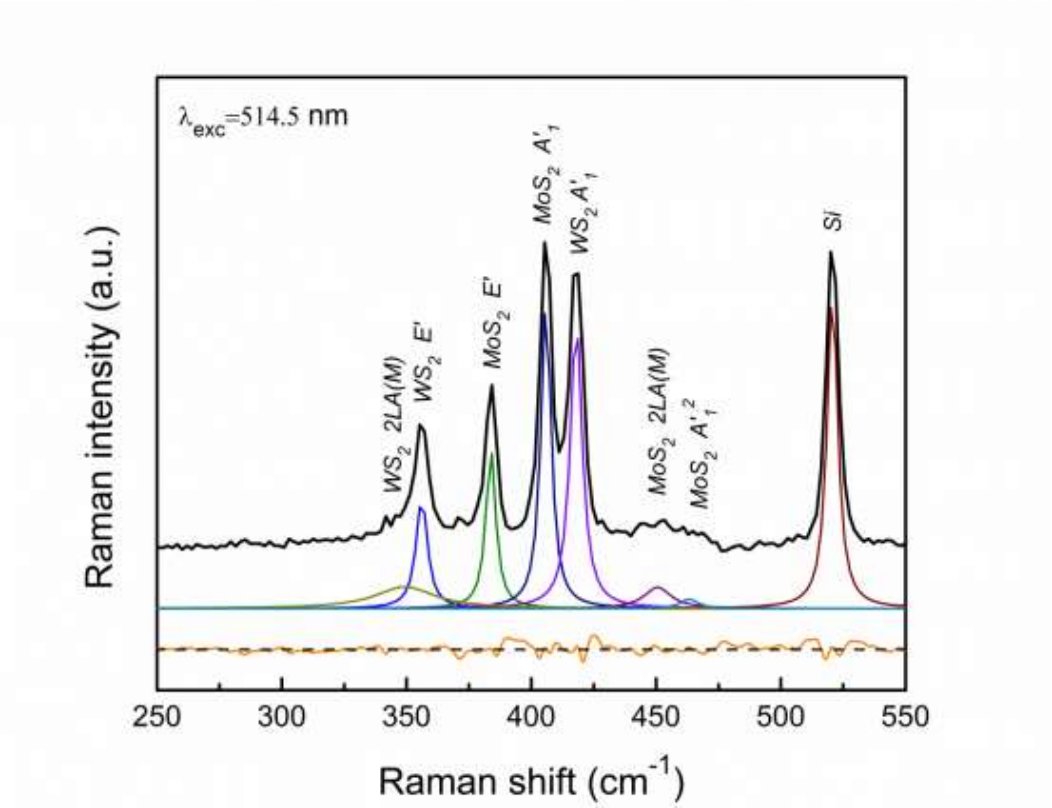

Figure S10. Fitting and indexing the Raman peaks in the Raman Spectra #4 in Fig. 3B.

The orange curve is the residual of the fitting.

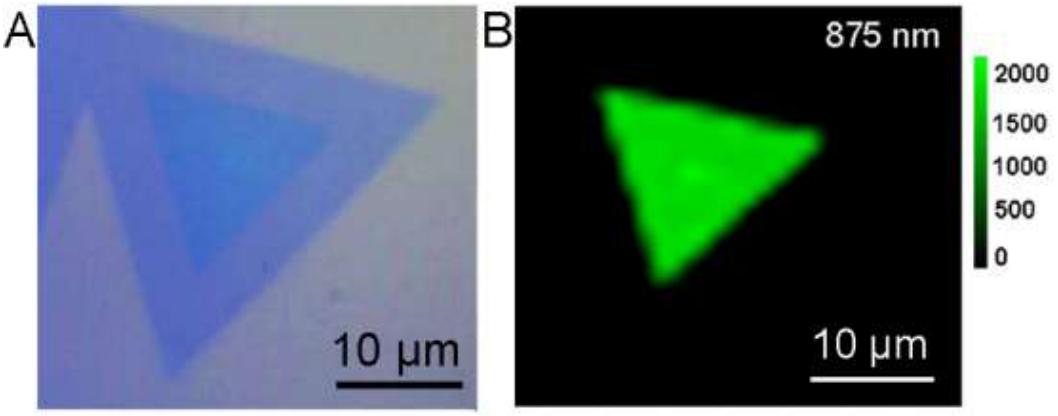

Figure S11. The PL intensity mapping at 875 nm of WS_2/MoS_2 stacked bilayer, confirming the intensity is localized at the bilayer region.

DOI: 10.1038/NMAT4091

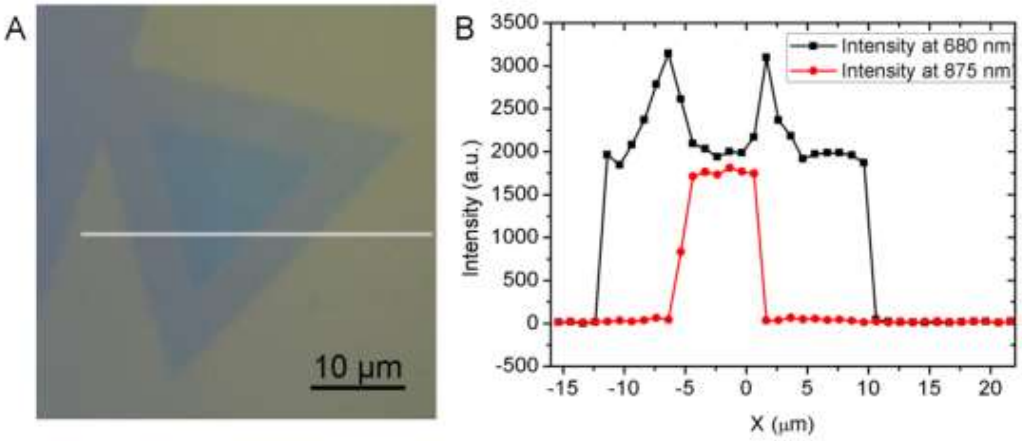

Figure S12. PL intensity line profile. (A) Optical image of the WS_2/MoS_2 vertical heterostructure, as shown in Fig. 3E in the main text. (B) PL intensity line profile shows localized enhancement of the PL intensity at 680 nm near the step edges, and the interlayer excitonic transition (PL peak at 875 nm) are localized at the bilayer region.

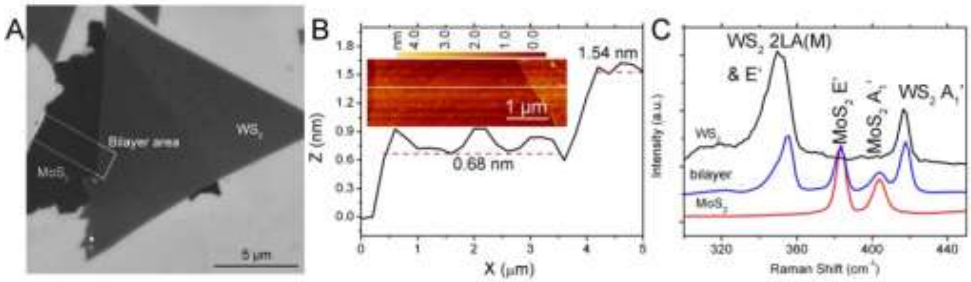

Figure S13. SEM image, AFM image and Raman spectra of the arbitrarily stacked WS_2/MoS_2 bilayer heterostructure prepared by mechanical transfer. (A) SEM image of the transferred sample, where the MoS_2 monolayer, WS_2 monolayer and their overlapping bilayer areas are marked. The area highlighted by white rectangle was further measured by AFM height topographies (inset in (B)). (B) Height profile along the white line in the inset, showing both MoS_2 and WS_2 are monolayer. (C) Corresponding Raman spectra from the MoS_2 monolayer, WS_2 monolayer and their overlapping bilayer. Raman spectra are sensitive to the quality of the film, substrate effect, and the external environment. Comparing with monolayer WS_2 on SiO_2/Si substrate, the peaks of WS_2 on MoS_2 always have shift and changed ratio, which can be attributed the substrate effect. Moreover, the MoS_2 and WS_2 monolayers used in making the transferred stacks here are synthesized individually through slightly different CVD processes. In addition, the physical stacking process of the two monolayers would inevitably introduce contaminations between the layers, while the direct growth of the MoS_2/WS_2 heterostack preserves a contamination-free interface. These differences give rise to the slightly different Raman intensity to the ones shown in Fig. 3B.

DOI: 10.1038/NMAT4091

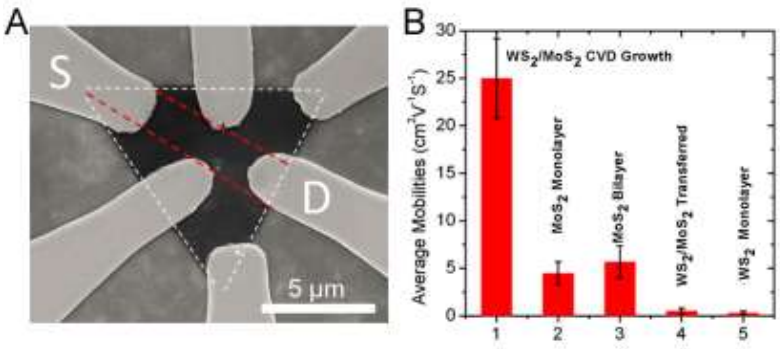

Figure S14. Field-effect transistor (FET) characterization of the vertical stacked WS_2/MoS_2 bilayer. (A) A typical SEM image of FET device from WS_2/MoS_2 bilayer stacks. (B) Histogram of the average mobility of CVD-grown WS_2/MoS_2 bilayer, mechanically transferred WS_2/MoS_2 bilayer, MoS_2 bilayer, and monolayer MoS_2, respectively. 10 devices are used to calculate the average mobility in each case.

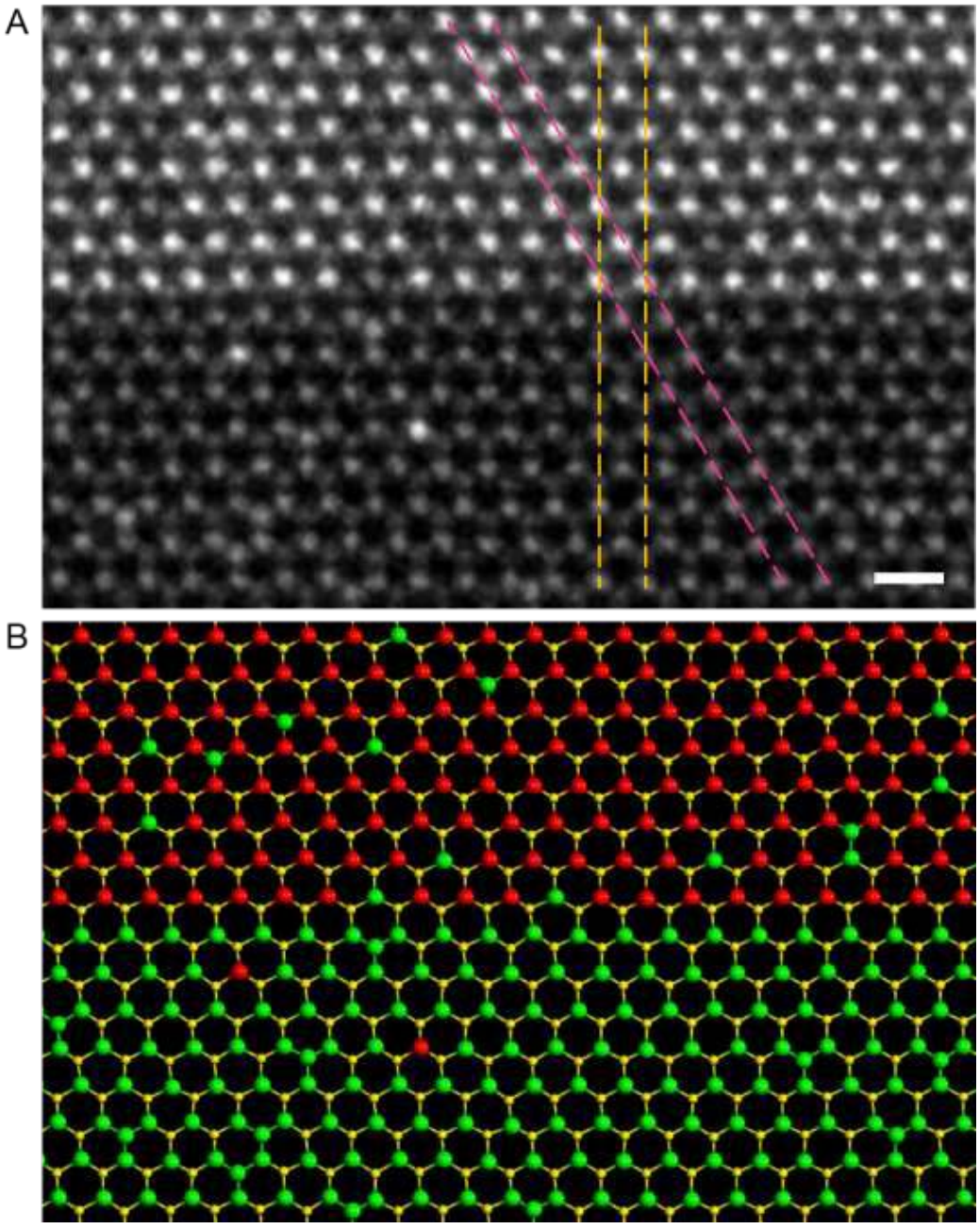

Figure S15. Seamless connection of the MoS_2 and WS_2 at the interface. (A) High resolution STEM Z-contrast image of the lateral interface where all atoms are clearly visible. The orange and pink dashed lines depict the atomic planes along the arm-chair and zigzag directions, respectively, which further illustrate that the WS_2 and MoS_2 regions share the same crystal orientation. (B) Atom-by-atom mapping of (A). Green: Mo; Red: W; Yellow: S. Scale bar: 0.5 nm.

DOI: 10.1038/NMAT4091

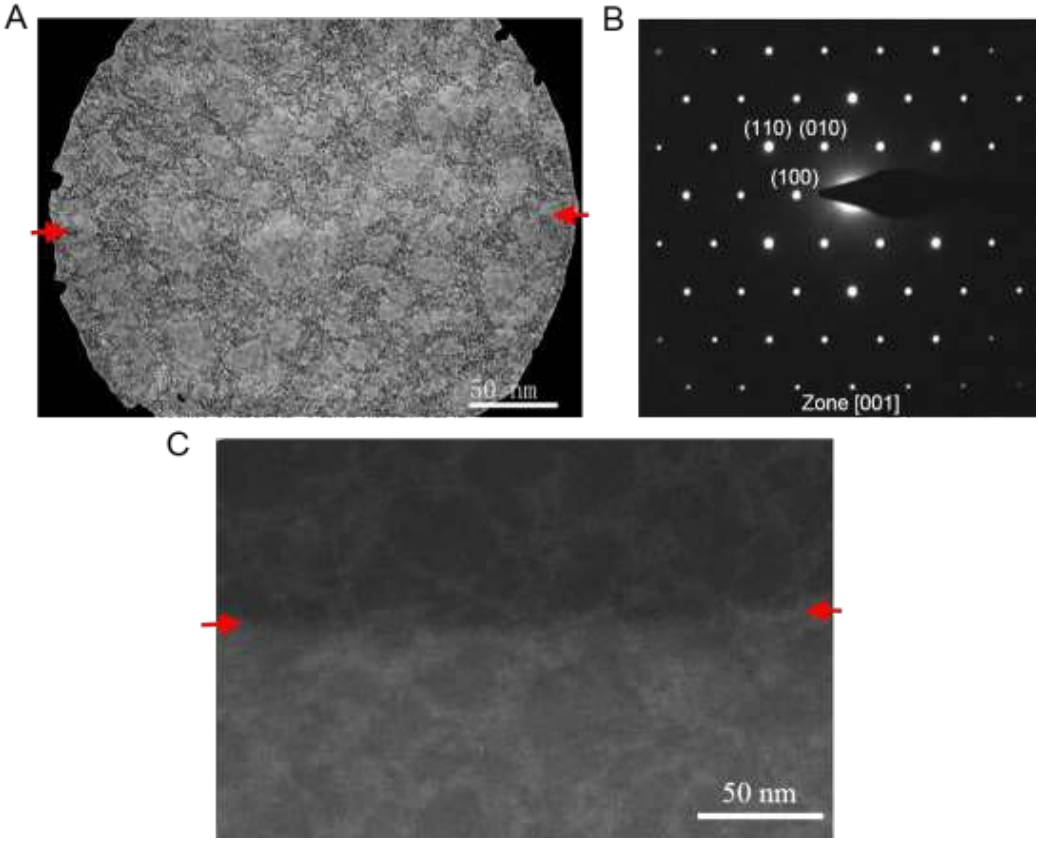

Figure S16. Electron diffraction pattern of a 300 nm region containing a lateral interface. (A) TEM bright field image with selected area aperture. (B) Electron diffraction pattern taken from (A) showing only one set of diffraction. (C) Low magnification STEM Z-contrast image of the same area. The position of the interface is indicated by the red arrows.

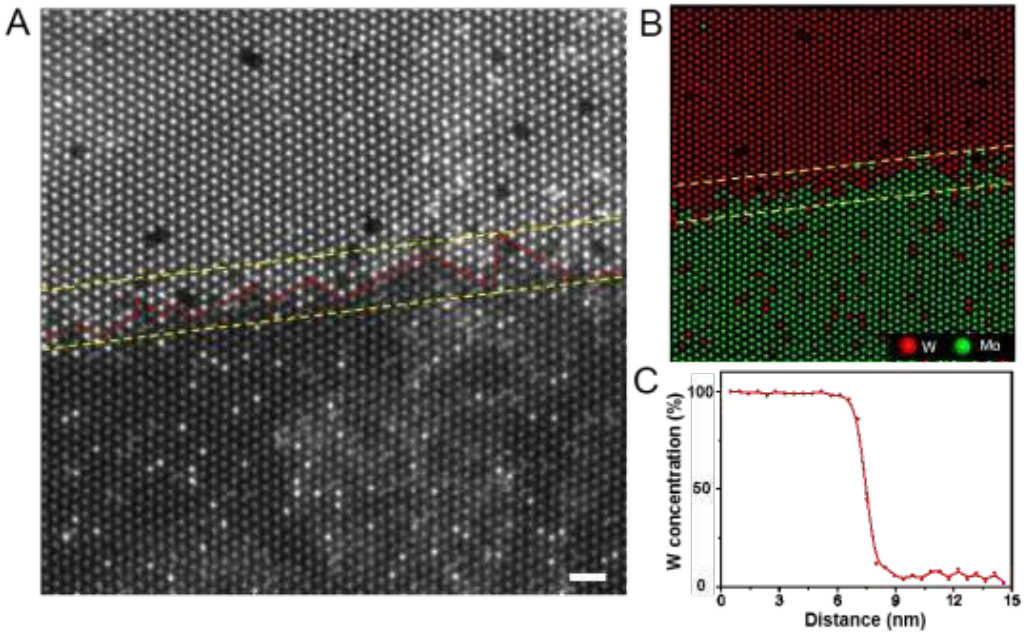

Figure S17. Atom-by-atom analysis of the lateral WS_2-MoS_2 interface. (A) Z-contrast STEM image of the in-plane boundary between MoS_2 and WS_2 domains as shown in Fig. 4A (main text), with a larger view. The yellow dashed lines indicate the roughness of the interface. (B) Atomic mapping of the Mo and W atoms distribution in (A). (C) W concentration estimated along the axis perpendicular to the yellow dashed line (the overall direction of the interface), which averages the W concentration in each individual atomic plane. The width of the boundary is estimated to be within 4 unit cells. The Mo concentration in the WS_2 side is ~ 0.2%, while the W in the MoS_2 side is ~ 7.4%. Scale bar: 1 nm.

DOI: 10.1038/NMAT4091

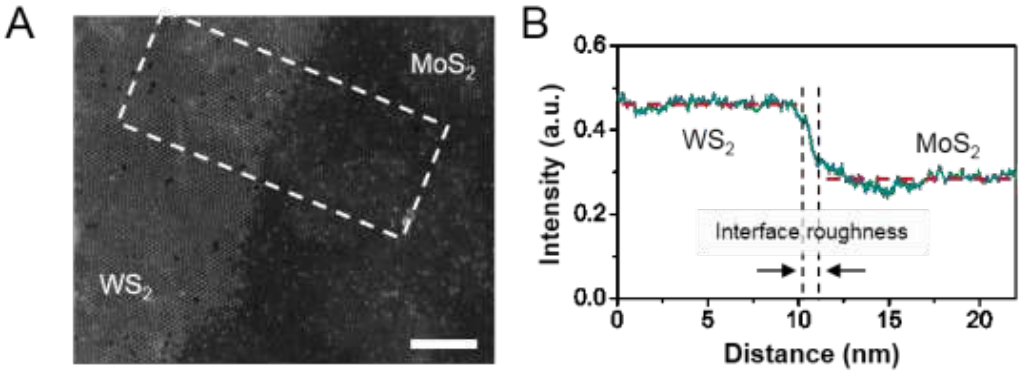

Figure S18. Overall morphology of the lateral interface between the MoS_2 and WS_2 domains. (A) Low-magnified STEM Z-contrast image of the interface between MoS_2 and WS_2 domain. (B) Line intensity profile integrated along the white dashed rectangle in (A), where the width of the intensity change is estimated to within 1 nm. Scale bar: (A) 5 nm.

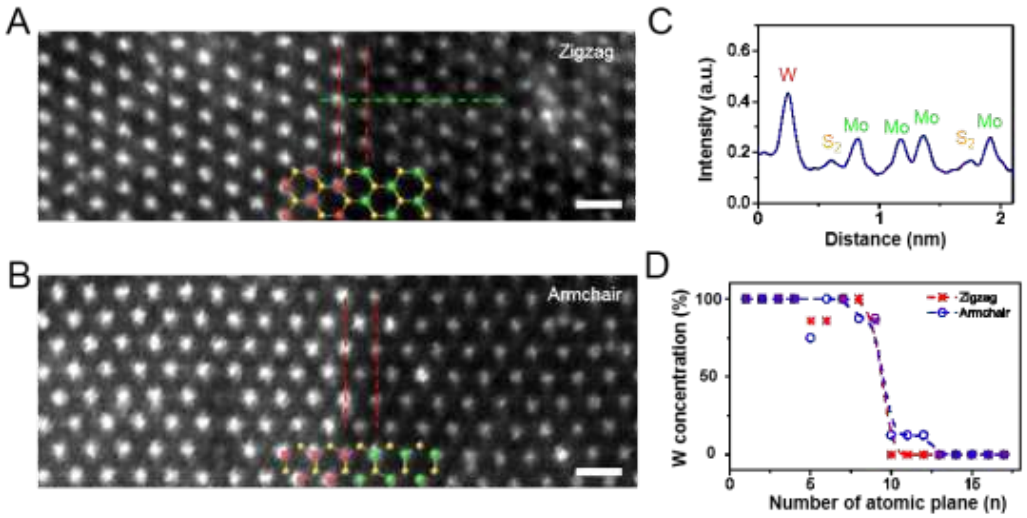

Figure S19. Chemical analysis of the lateral interface along the zigzag and armchair directions. (A, B) Atomic resolution Z-contrast images of the atomically sharp in-plane WS_2-MoS_2 interface along zigzag (A) and armchair (B) directions. (C) Intensity profile of different atomic species along the green dashed line in (A). Mo_{S2} substitution defects are observed near the interface, suggesting a Mo-rich environment during the growth. (D) Local W concentration across the interfaces shown in A and B. The W concentration was integrated along zigzag and armchair directions as indicated by the red dashed lines in (A, B), respectively. The dashed lines are guide to eyes. Scale bars: 0.5 nm.

DOI: 10.1038/NMAT4091

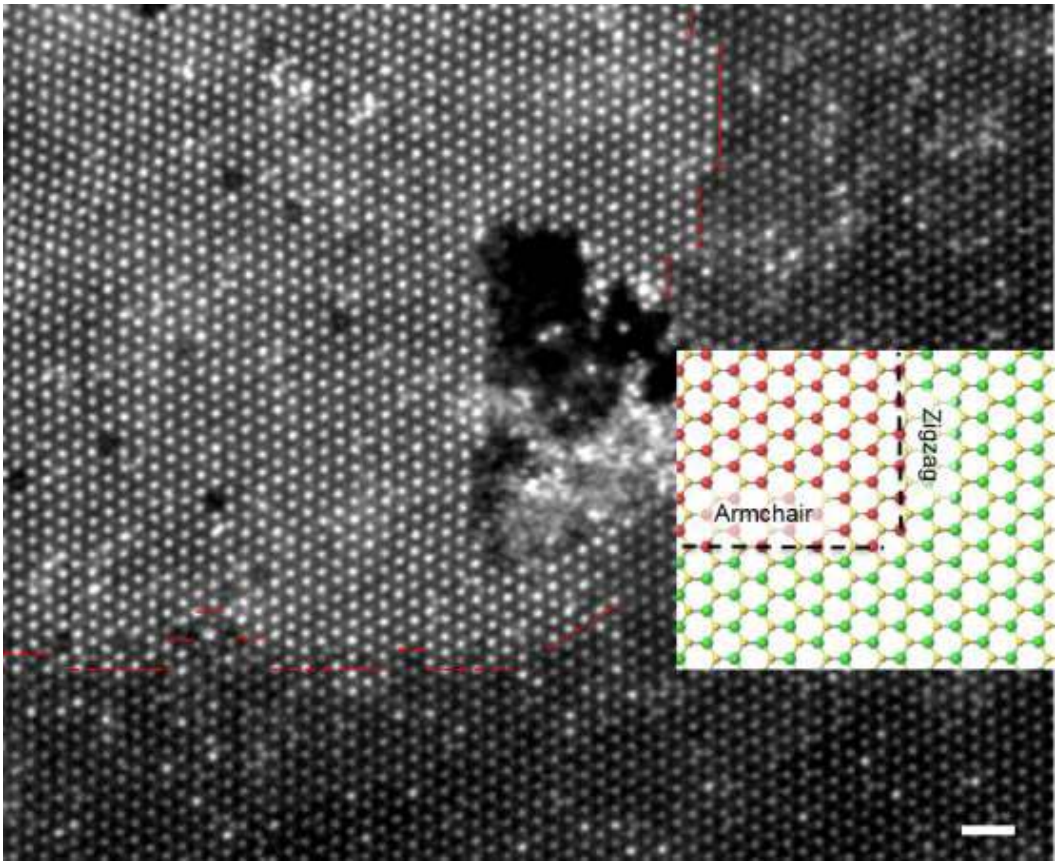

Figure S20. Coexistence of lateral WS_2-MoS_2 interfaces along the armchair and zigzag directions. The red dashed lines highlight the interfacial steps along both the zigzag and armchair directions. The WS_2 domain grows epitaxially along the edges of the MoS_2 monolayer, forming lateral interfaces along both directions. Inset: Schematic of the interface along zigzag and armchair direction, respectively. Scale bar: 1 nm.

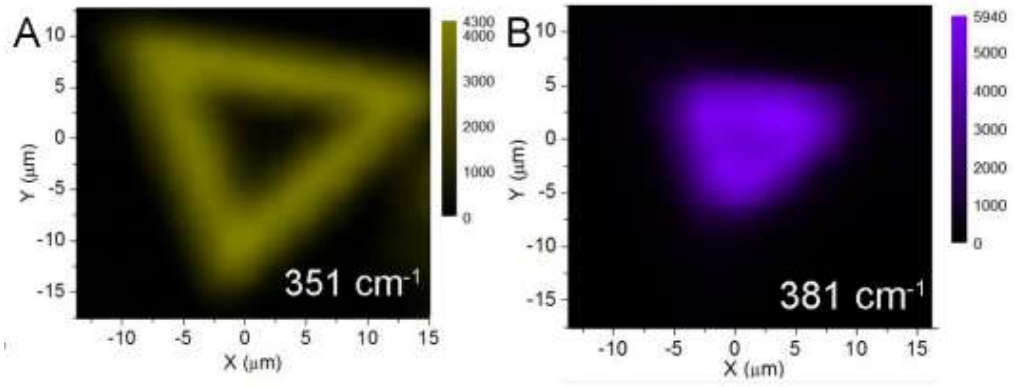

Figure S21. Raman mapping of the WS_2-MoS_2 in-plane heterojunction. (A) and (B) are Raman intensity maps at 351 cm^{-1} and 381 cm^{-1}, respectively, from the heterostructure shown in Figure 5A in the main text.

DOI: 10.1038/NMAT4091

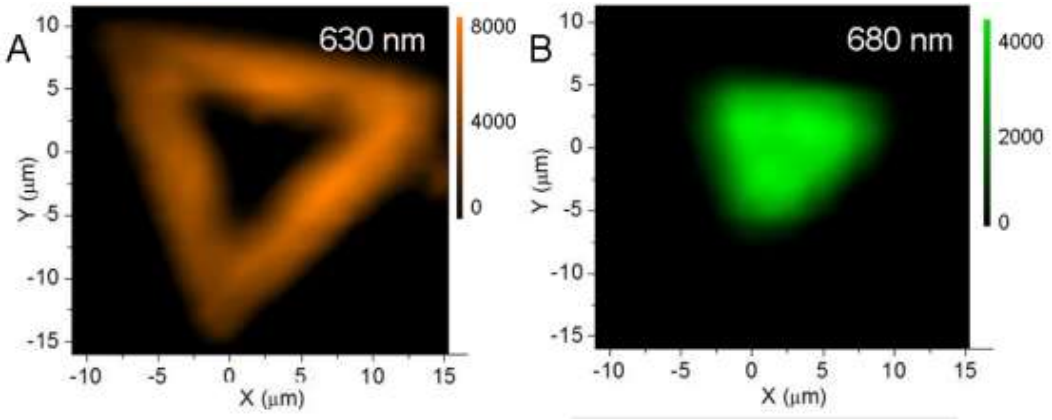

Figure S22. PL mapping of WS_2-MoS_2 in-plane heterostructure. (A) and (B) are PL intensity mapping at 630 nm and 680 nm, respectively, acquired from the heterostructure shown in Figure 5A in the main text.

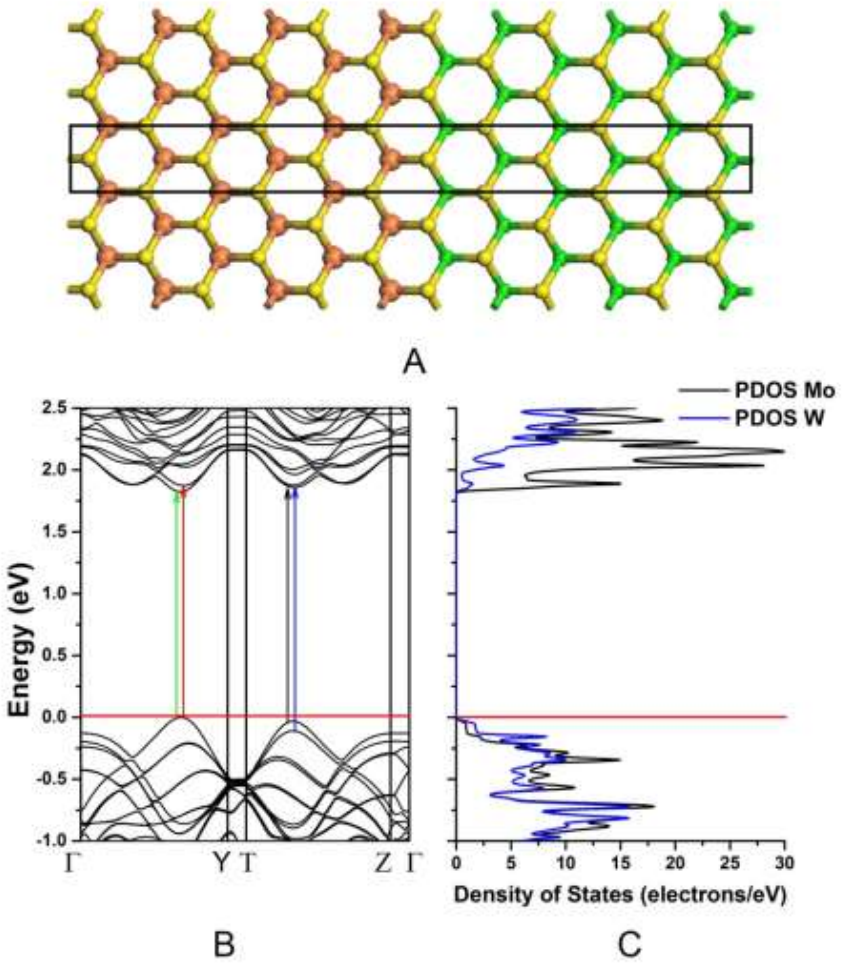

Figure S23. Zigzag WS_2/MoS_2 monolayer interface. (A) Model showing the unit cell used in the DFT calculations with tungsten atoms in orange (bigger atoms), sulfur in yellow and molybdenum in green. (B) Band structure of the cell in (A) showing direct transitions at 1.825 eV (679 nm. Green arrow), 1.875 eV (661.33 nm. Red arrow), 1.889 eV (656.43 nm. Black arrow), 1.908 eV (649.89 nm. Not shown), 1.968 eV (630.08 nm. Blue arrow), 1.987 eV (624.05 nm. Not shown). The red horizontal line shows the top of the valence band. (C) Partial Density of States contributed by Mo and W atoms.

DOI: 10.1038/NMAT4091

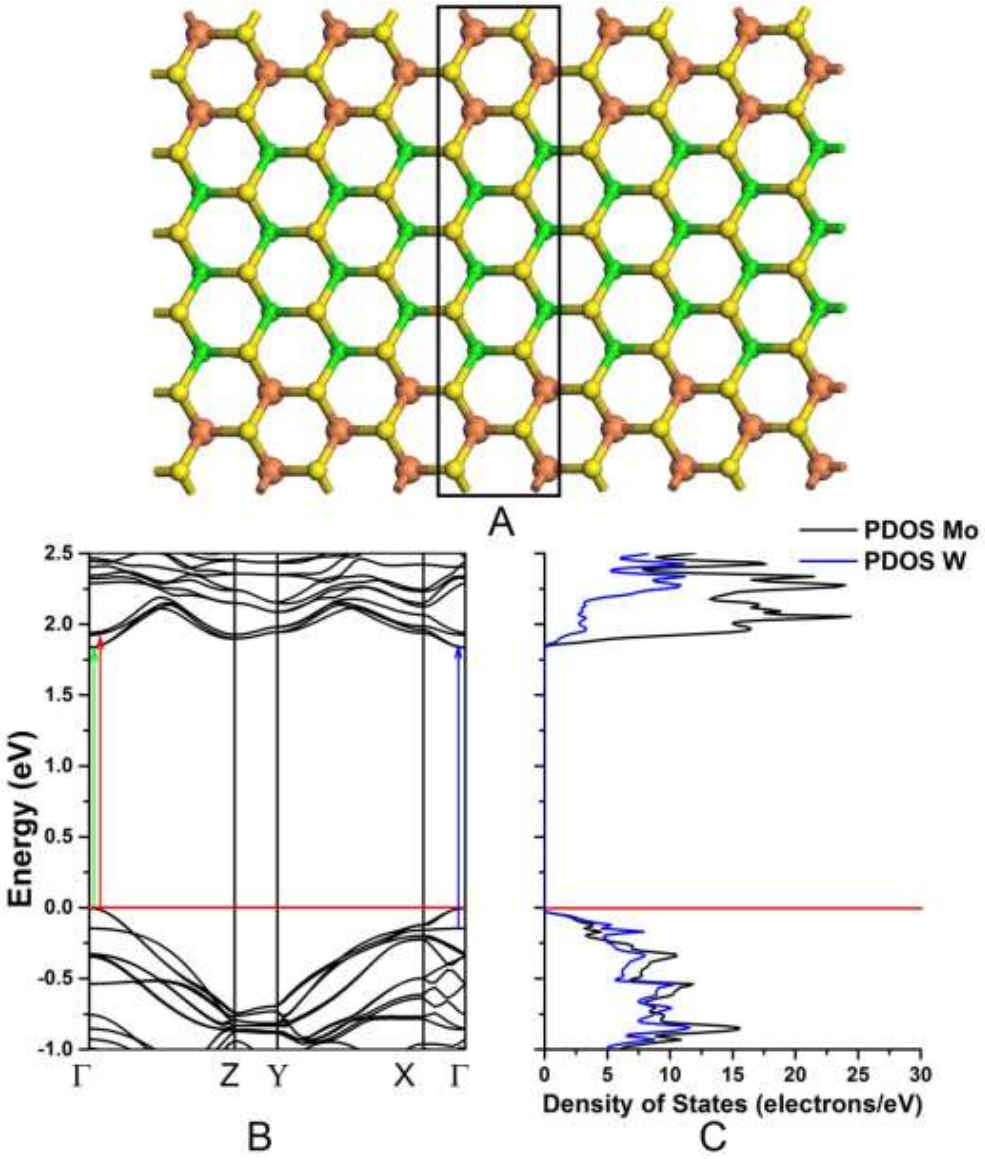

Figure S24. Armchair WS_2/MoS_2 monolayer interface. (A) Model showing the unit cell used in the DFT calculations with tungsten atoms in orange (bigger atoms), sulfur in yellow and molybdenum in green. (B) Band structure of the cell in (A) showing direct transitions at 1.835 eV (675.74 nm. Green arrow), 1.925 eV (644.15 nm. Red arrow), 1.939 eV (639.50 nm. Not shown), 1.978 eV (626.89 nm. Blue arrow), 2.06 eV (599.61nm. Not shown). The red horizontal line shows the top of the valence band. (C) Partial Density of States contributed by Mo and W atoms.

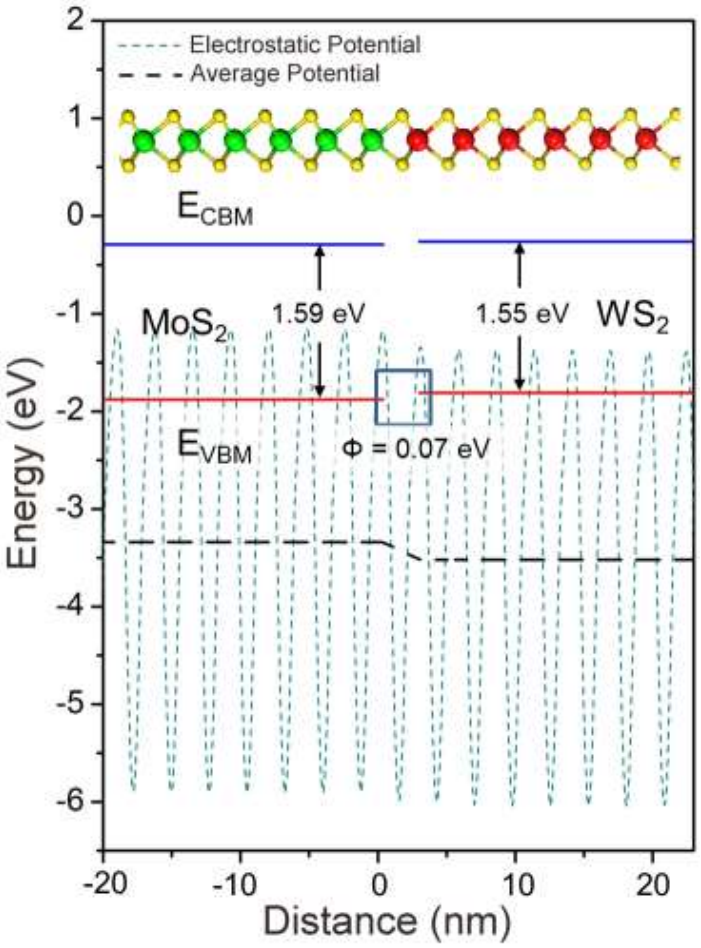

Figure S25. Band alignment in the lateral WS_2-MoS_2 heterojunction using electrostatic potential calculated by DFT. The band alignment was calculated using the electrostatic potential as a reference, where the change of the average electrostatic potential through the interface is calculated using a WS_2-MoS_2 heterojunction, and the valence-band-maximum (E_{VBM}) of the two semiconductors with respect to the electrostatic potential are calculated using the individual monolayer unit cell[17]. The band alignment is found to be a type II heterojunction (staggered gap), similar to the result reported by in literature[18]. The bandgap is found to mismatch by a value of 0.07 eV, which is enough for the separation of electron-hole pairs and the occurrence of photo-voltaic effect in room temperature. Although the bandgap mismatch is small, such small change of the bandgap occurs in a single atomic row (~ 3 Å in width), which gives a strong built-in electric field of over 2×10^8 N/C. Such strong electric field may drive the free electrons and holes generated in the vicinity of the interface to recombine preferentially at the interface.

DOI: 10.1038/NMAT4091

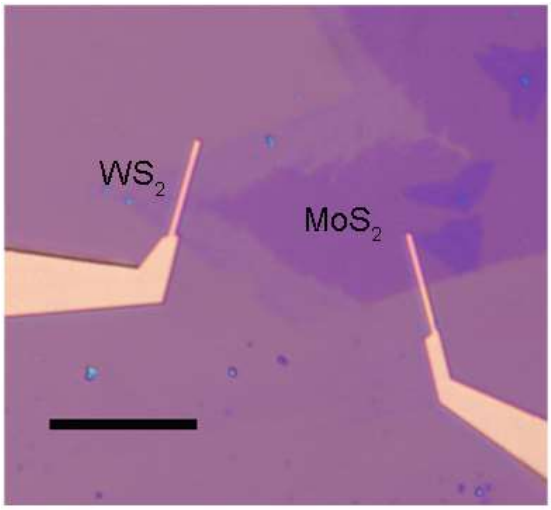

Figure S26. A typical optical image of device based on WS_2-MoS_2 in-plane heterojunction, where one electrode is on the outer layer WS_2 and the other one is placed on the inner layer MoS_2. Scale bar: 10 μm.

Reference:

1 van der Zande, A. M. *et al.* Grains and grain boundaries in highly crystalline monolayer molybdenum disulphide. *Nature Mater.* **12**, 554-561 (2013).

2 Najmaei, S. *et al.* Vapour phase growth and grain boundary structure of molybdenum disulphide atomic layers. *Nature Mater*. **12,** 754-759 (2013).

3 Zhou, H. Q. *et al.* Thickness-dependent patterning of MoS_2 sheets with well-oriented triangular pits by heating in air. *Nano Res* **6**, 703-711 (2013).

4 Clark S J, S. M. D., Pickard C J, Hasnip P J, Probert M J, Refson K, Payne M C. First principles methods using CASTEP Z. *Kristallogr.* **220**, 567-570 (2005).

5 Ceperley, D. M. & Alder, B. J. Ground-state of the eectron-gs by a sochastic mthod. *Phys. Rev. Lett.* **45**, 566-569 (1980).

6 Perdew, J. P. & Zunger, A. Self-interaction correction to density-functional approximations for many-electron systems. *Phys. Rev. B* **23**, 5048-5079 (1981).

7 Wei, X. L. *et al.* Modulating the atomic and electronic structures through alloying and heterostructure of single-layer MoS_2. *J Mater. Chem. A* **2**, 2101-2109 (2014).

8 Grimme, S. Accurate description of van der Waals complexes by density functional theory including empirical corrections. *J. Comput. Chem.* **25**, 1463-1473 (2004).

9 Milman, V. *et al.* Electronic structure, properties, and phase stability of inorganic crystals: A pseudopotential plane-wave study. *Int. J. Quantum Chem.* **77**, 895-910 (2000).

10 Liu, Y., Bhowmick, S. & Yakobson, B. I. BN White Graphene with "Colorful" Edges: The Energies and Morphology. *Nano Lett.* **11**, 3113-3116.

11 Kang, J., Tongay, S., Li, J. B. & Wu, J. Q. Monolayer semiconducting transition metal dichalcogenide alloys: Stability and band bowing. *J. Appl. Phys.* **113**, 143703 (2013).

12 Sargent, A. L., Hall, M. B. & Guest, M. F. Theoretical-studies of inorganic and organometallic reaction-mechanisms .3. The origin of the difference in the barrier for the kinetic and thermodynamic products for the oxidative addition of dihydrogen to a square-planar iridium complex. *J. Am. Chem. Soc.* **114**, 517-522 (1992).

13 Gutierrez, H. R. *et al.* Extraordinary room-temperature photoluminescence in triangular WS_2 monolayers. *Nano Lett.* **13**, 3447-3454 (2013).

14 Chen, Y. *et al.* Tunable Band Gap Photoluminescence from Atomically Thin Transition-Metal Dichalcogenide Alloys. *ACS Nano* **7**, 4610-4616 (2013).

15 Okamoto, H. Tellurium-Tungsten Binary Diagram. *ASM Alloy Phase Diagrams Center, P. Villars, editor-in-chief; H. Okamoto and K. Cenzual, section editors;* http://www1.asminternational.org/AsmEnterprise/APD, (1900).

16 Gong, Y. *et al.* Band gap engineering and layer-by-layer mapping of selenium-doped molybdenum disulfide. *Nano Lett.* **14**, 442-449 (2014).

17 Delaney, K. T., Spaldin, N. A. & Van de Walle, C. G. Theoretical study of Schottky-barrier formation at epitaxial rare-earth-metal/semiconductor interfaces. *Phys. Rev. B* **81**, 165312 (2010).

18 Kang, J., Tongay, S., Zhou, J., Li, J. & Wu, J. Band offsets and heterostructures of two-dimensional semiconductors. *Appl. Phys. Lett.* **102**, 012111 (2013).